Journal of Nuclear Materials 397 (2010) 122–127

Contents lists available at ScienceDirect

Journal of Nuclear Materials

journal homepage: www.elsevier.com/locate/jnucmat

Precipitation behavior of Xe at grain boundaries in Si_3N_4 ceramic during implantation at elevated temperature

Yoon-Uk Heo [a,b,*], Masaki Takeguchi [a,b], Kazutaka Mitsuishi [b,c], Minghui Song [a,b], Yoshiko Nakayama [b], Kazuo Furuya [d]

[a] Advanced Nano-characterization Center, National Institute for Materials Science, 3-13 Sakura, Tsukuba 305-0003, Japan
[b] High Voltage Electron Microscopy Station, National Institute for Materials Science, 3-13 Sakura, Tsukuba 305-0003, Japan
[c] Quantum Dot Research Center, National Institute for Materials Science, 3-13 Sakura, Tsukuba 305-0003, Japan
[d] NIMS Center for Nanotechnology Network, National Institute for Materials Science, 3-13 Sakura, Tsukuba 305-0003, Japan

ARTICLE INFO

Article history:
Received 22 May 2009
Accepted 25 December 2009

ABSTRACT

Upon implantating of Xe ions into silicon nitride ceramic at 800 °C, the precipitation of Xe at grain boundaries (GBs) was observed. Transmission electron microscopy, high-angle annular dark-field scanning transmission electron microscopy, and electron energy-loss spectroscopy analyses showed that the precipitates at GBs were amorphous Xe nanoparticles. The Xe precipitates grew and coalesced with each other upon post implantation annealing. Crack paths that formed in the samples due to ex situ mechanical stress with and without Xe implantation were also investigated, and the change in crack paths by the presence or the evaporation of Xe precipitates at GB was confirmed.

© 2009 Elsevier B.V. All rights reserved.

1. Introduction

The noble-gas ion implantation method has been used to study the effects of particle irradiation on metals [1–8] and ceramics [9–14]. Various noble-gases such as He [3,5], Ar [7], Ne [4,7,12], Kr [8,13], and Xe [1,2,6,7,9–12] have been used as sources of implantation ions. Among them, the heavy noble-gases such as Kr and Xe have so large atomic sizes that can generate displacement damage in the matrix during the implantation and the substitutional sites or voids of lattice can be used for the diffusion of these ions in the matrix. This is different with the case of the light element, i.e., He, where the interstitial sites of lattice can also be the diffusion paths. Therefore, Xe would be the best ion source for the investigating the effect of the heavy ion implantation in the materials due to the large ion size. Studies on Xe implantation have extensively focused on the behavior of crystalline and amorphous precipitation in the metallic matrix after implantation [1,6,15]. It was considered that the main factor determining the crystalline or amorphous state of implanted Xe is the pressure inside Xe particles, which is related to the Xe particle size, the Xe/matrix surface energy, and the shear modulus of the matrix [1,7,15]. Actually, the bonding property of the matrix also plays an important role in determining the pressure in the Xe precipitate. However, there have been few reports on the crystallization of Xe particles in ceramics except for MgO, although crystalline Xe particles often form in metallic matrices, because of the difference between the metallic bonding in the metallic matrix and the covalent bonding in the ceramic matrix [9,13,14].

In previous studies, the effect of noble-gas ion implantation on mechanical properties was discussed from the viewpoints of irradiation-induced phase transformations and the generation of defect in metals [2–4] and ceramics [11,12,14]. In the case of metals, there have been a large number of studies on irradiation-induced defects because the crystalline structure of a metal is likely to be retained after irradiation at room temperature, and therefore the defects can be easily characterized. However, this is not the case for ceramics. Regarding for the precipitation of a noble-gas at grain boundaries (GBs), although there have been a limited number of reports on metallic matrices [6], to the best of our knowledge, no atomic-scale research on ceramic matrices has yet been carried out.

Most of ceramic materials are destroyed the crystalline structure to amorphous by ion irradiation at room temperature [14]. This makes difficult to investigate the defects, secondary phase, and GBs after ion implantation in the ceramic materials. However, the crystal structure of the ceramic materials is preserved at the elevated temperature after ion implantation, because the recovery of damaged matrix occurs at the high temperature. Besides, the elevated temperature accelerates the diffusion process of the implanted ion in the matrix. Therefore, the implantation at the elevated temperature will be helpful to understand the behavior of the implanted ion in a crystalline ceramic matrix. In this study,

* Corresponding author. Address: Advanced Nano-characterization Center, National Institute for Materials Science, 3-13 Sakura, Tsukuba 305-0003, Japan. Tel.: +81 029 863 5548; fax: +81 029 863 5586.
E-mail addresses: YOONUK.Heo@nims.go.jp, yunuk01@snu.ac.kr (Y.-U. Heo).

0022-3115/$ - see front matter © 2009 Elsevier B.V. All rights reserved.
doi:10.1016/j.jnucmat.2009.12.018

we investigate the precipitation behavior of Xe at GBs in polycrystalline Si_3N_4 ceramic, which is a representative structural ceramic, after irradiation by Xe ions at 800 °C by transmission electron microscopy (TEM), high-angle annular dark-field scanning TEM (HAADF-STEM), and electron energy-loss spectroscopy (EELS). Crack paths that formed due to ex situ mechanical stress in the samples with and without Xe implantation are also observed. On the basis of our observations, the effect of Xe precipitation at GBs on the fracture strength is discussed.

2. Experimental procedure

TEM samples were prepared from bulk silicon nitride (Si_3N_4, 98.53 wt.% purity, Fe content 0.2 wt.%, O content 0.98 wt.%, Ca content 0.04 wt.%, C content 0.09 wt.%, Al content 0.15 wt.%) of the Kyocera Corporation (Lot number 1061; 1-1 Kokubuyamashita-co, Kirishima, Kagoshima 899-4396, Japan) by cutting, mechanical polishing, and ion milling using a Gatan 691 precision ion polishing system (PIPS™). The Si_3N_4 samples were polycrystalline with both small grains (0.1 μm–0.5 μm) and large grains (10 μm–20 μm), and were composed of α- and β-phases which was confirmed by X-ray powder diffraction measurement using a Cu-K_α source.

Xe ions with an energy of 100 keV were irradiated onto the TEM samples within 2 mm diameter range with a dose of 2×10^{16} ions/cm^2 at 800 °C for 26 min in a JEOL high-voltage electron microscope (ARM-1000) equipped with a dual ion implantation system [16]. The projected range of 100 keV Xe ion in the Si_3N_4 matrix calculated using the Monte Carlo simulation program SRIM [17]. The results of the calculation showed that the peak concentration located about 33 nm depth from the projected surface with a longitudinal straggling of about 7 nm with about 41 displacements per atom (dpa). The maximum Xe concentration at the dose of 2×10^{16} ions/cm^2 was about 1×10^{14} Xe/cm^3 at a sample depth of 33 nm.

TEM observations were performed. Some samples were annealed in the microscope at 800 °C for 30 min to cause the Xe precipitates to grow after irradiation. To enable a comparison between the fracture behavior before and after Xe irradiation, samples annealed at 800 °C for 56 min without Xe irradiation were also characterized.

The elemental mapping of Xe was performed by an energy-filtering TEM (EFTEM) technique in a JEOL 300 keV field-emission transmission electron microscope (JEM-3000F) equipped with a Gatan 863 energy filter (GIF Tridiem). EFTEM images were obtained using Xe-$M_{4,5}$ edge loss electrons with a 40 eV slit width.

HAADF-STEM and STEM-EELS were also performed to obtain Z-contrast images and sub-nanometer probe EEL spectra using a JEOL Cs-corrected dedicated STEM (JEM-2500SES) equipped with a Gatan 766 EELS spectrometer (Enfina 1000) under the conditions of an HAADF detector inner cutoff angle in 133 mrad, and an EEL spectra acquisition angle of 22 mrad, respectively. The thickness of thin foil was measured using EEL spectra in Xe-irradiated sample. Kramers–Kronig sum rule was applied to the calculation and the error range of this method was reported below 10% [18].

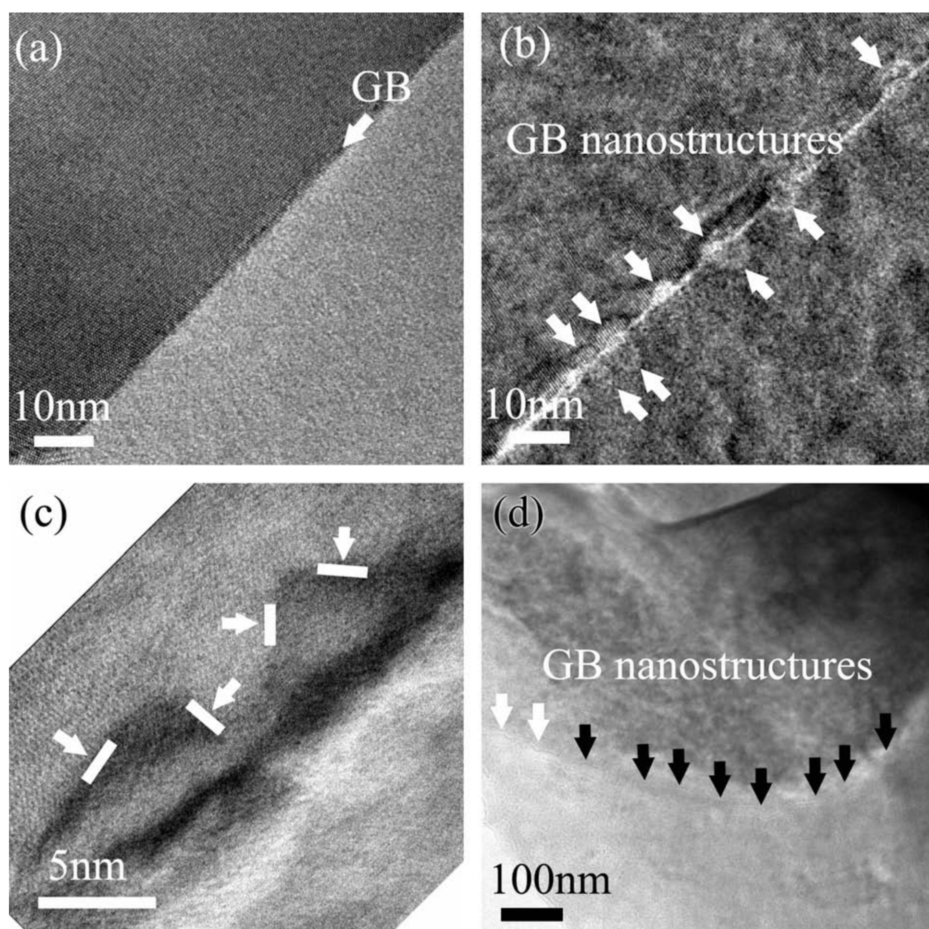

Fig. 1. TEM images of Si_3N_4 grain boundary: (a) before Xe irradiation, (b) after Xe irradiation at a dose of 2×10^{16} ions/cm^2 at 800 °C, (c) high-magnification image of (b) and (d) grain boundary after post irradiation annealing for 30 min at 800 °C. GB nanostructures are indicated by arrows in b–d.

To investigate the detrimental effect of Xe irradiation on the fracture strength of the samples, the crack morphologies of samples annealed at 800 °C with and without Xe irradiation were observed using a JEOL field-emission scanning electron microscope (SEM, JEM-6700F). For clear observation of the GBs, both samples were slightly etched by 30 keV Ga ions by scanning in a JEOL focused-ion-beam machine (JEM-9310FIB) for 15 min after fracture.

3. Results

3.1. Precipitation of Xe nanoparticles at GBs

Fig. 1a and b shows TEM images of a Si_3N_4 GB before and after Xe irradiation at a dose of 2×10^{16} ions/cm^2 at 800 °C, respectively. There are no nanostructures at the GB before Xe irradiation as shown in Fig. 1a. The contrast difference between the two grains on other sides of the GB in Fig. 1a is due to the difference in crystallographic orientation. After the Xe irradiation, some irregularly shaped nanostructures with a size of 5–10 nm appeared at the GB as indicated by white arrows in Fig. 1b. A high-magnification image of these nanostructures is displayed in Fig. 1c. The nanostructures are faceted, as marked with white arrows. The lattice fringes of the Si_3N_4 matrix were clearly observed, whereas no additional fringes originating from the nanostructures were observed. Furthermore, nano beam (beam size; 7 nm) diffraction patterns obtained from the nanostructures indicated no extra spots other than those from the Si_3N_4 matrix. These results suggest that the nanostructures that appeared are amorphous or voids. These nanostructures increased in size to about 20–50 nm after annealing for 30 min at 800 °C (Fig. 1d). In Fig. 1d, the contrast of some of the nanostructures (those marked with white arrows) became brighter while others retained the same contrast.

To determine the composition of the nanostructures appearing at the GB, EFTEM mapping was performed. Fig. 2a and c shows EFTEM zero-loss images of the GB regions in thick and thin areas of the samples after annealing, respectively. The corresponding EFTEM maps of the Xe-$M_{4,5}$ edge are respectively shown in Fig. 2b and d. Because of the thickness of the sample, the contrast of the nanostructures and the corresponding Xe maps are not high, but it is clear that the element comprising the nanostructures is Xe. On the other hand, there are two types of contrast in the nanostructures as indicated by the white and black arrows in Fig. 2c; i.e., bright and faint contrast, respectively. The corresponding Xe map in Fig. 2d clearly indicates that the nanostructures with the faint contrast are Xe but those with the bright contrast are voids rather than Xe. EFTEM maps of the samples before annealing also show similar features. Thus, we can conclude that most of the nanostructures formed by Xe implantation at 800 °C are Xe, but others, which exhibit the bright contrast are voids.

Fig. 3a and b shows HAADF-STEM images of another area in the same sample as that used for the EFTEM observation in Fig. 2. HAADF-STEM images exhibit contrast that depends on the atomic number, so-called Z-contrast. In the figure, the GB is recognized by the nanostructures with both bright and dark contrast. The bright contrast is due to the existence of an element with a large atomic number, i.e., Xe. The dark contrast is attributed to not only

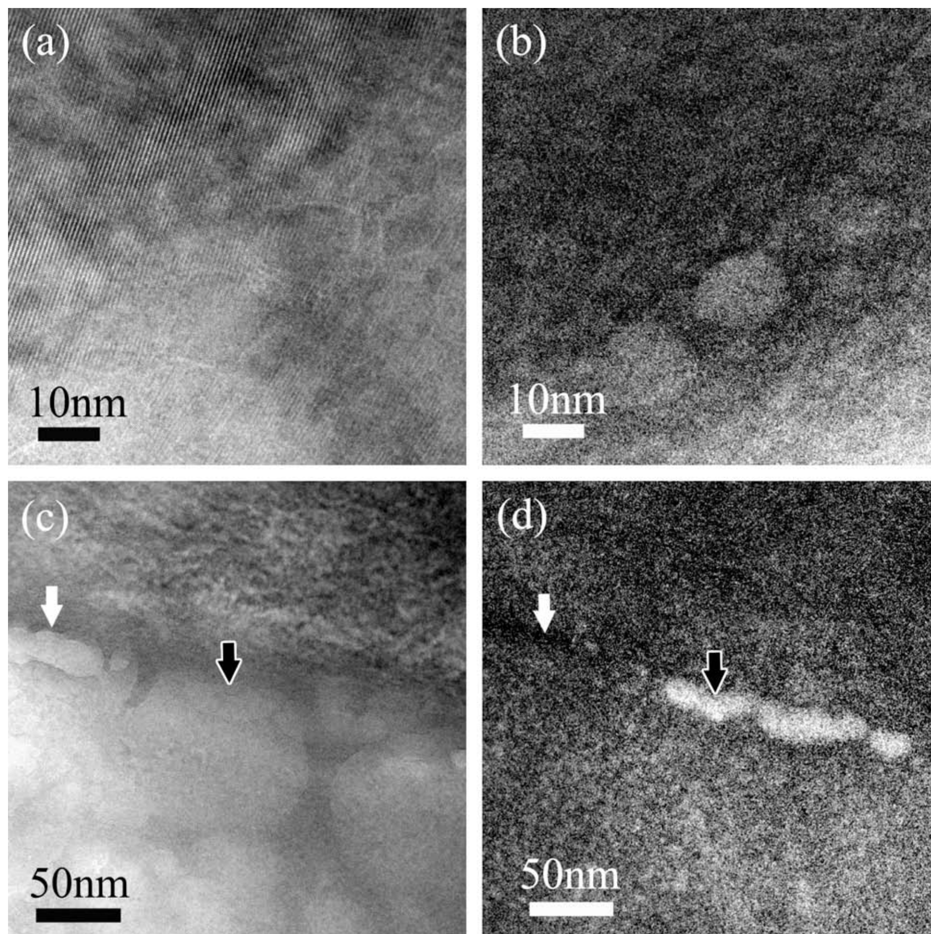

Fig. 2. EFTEM zero-loss images (a and c) and Xe-$M_{4,5}$ edge images (b and d) of the specimen after post irradiation annealing obtained using slit widths of 20 and 40 eV, respectively.

the absence of Xe but also the thinness of the sample. Therefore, it is deduced that the dark contrast is due to the existence of voids. In some areas, the GB is mainly represented by the dark contrast as indicated by the white arrow in Fig. 3b. This is recognized as a crack rather than voids.

Note that there are also Xe precipitates distributed in the grains, some of which are indicated by white arrows. They are much smaller than those precipitated at the GB. They were not detected by EFTEM because of their size.

Fig. 3c and d shows EEL spectra obtained from the positions denoted in Fig. 3a. Spectrum 2, obtained from a Xe precipitate at the GB (denoted by position 2), exhibits a clear Xe-$M_{4,5}$ peak, whereas the Xe-$M_{4,5}$ peak in spectra 1 and 3, obtained from the grains (denoted by positions 1 and 3), is faint. The intensity of the N–K peak in spectrum 2 is lower than that in spectra 1 and 3. This means that the precipitation of Xe occurs at the GB previously occupied by Si and N atoms. Spectrum 5, obtained from the dark contrast area in the GB (denoted by position 5), exhibits a faint Xe-$M_{4,5}$ peak. Xe evaporated from inside of sample when Xe precipitate grew and contacted to the sample surface.

From these EFTEM and STEM-EELS observations, we can conclude that Xe precipitates are formed by Xe ion implantation at a high temperature. The Xe precipitates are likely to grow preferentially at the GB but not in grains at a high temperature. If the grown Xe precipitates meet with the sample surface, Xe evaporates into the vacuum, resulting in the formation of voids. The fact that the voids and cracks were both clearly observed in the thin areas supports this conclusion.

3.2. Formation of Xe nanoparticles in a grain

Xe nanoparticles are formed in grains as well as at the GBs, as shown in Fig. 3a. To observe this in more detail, we broke the Xe-irradiated TEM sample using a diamond scriber. The single grain shown in Fig. 4 was investigated by HAADF-STEM. No Xe precipitates were detected at the GB in this case because they had evaporated. However, there were many Xe precipitates in the grain. In area 1, which is close to the GB, few Xe precipitates were appeared, and they were smaller than those in area 2. In area 2, some Xe precipitates (denoted by the black arrow) near the center of the grain increased in size by coalescing with adjacent Xe precipitates. This can be understood by considering that the Xe concentration is lower close to the GB (area 1) as a result of diffusion to the GB; thus, coalescence can only occur at the center region (area 2).

4. Discussion

4.1. Mechanism for precipitation of Xe particles at GB

Compared with the atomic radius of He, that of Xe is so large that only substitution with atoms or vacant sites in Si_3N_4 can occur in diffusion. This makes the diffusion of Xe atoms difficult at room temperature or low temperatures, even though Si_3N_4 itself has many defects such as dislocation loops and stacking faults [19]. However, there should be many equilibrium vacancies at an elevated temperature [20]. These vacancies could be precipitation sites as well as the paths of Xe diffusion in the Si_3N_4 matrix.

The mechanism of Xe precipitation in a grain and at a GB is displayed in Fig. 5. The implanted Xe atoms close to the GB diffuse to the GB to reduce the total free energy. It has been reported that large voids formed at the GBs of neutron-irradiated Si_3N_4 after annealing at 1500 °C for 1 h [21]. The preferential formation of voids and Xe precipitates at the GB in our experiments is good evidence of the diffusion of Xe to the GB. The Xe precipitates at the GB are faceted as shown in Fig. 1c. A study on the faceted plane of Xe

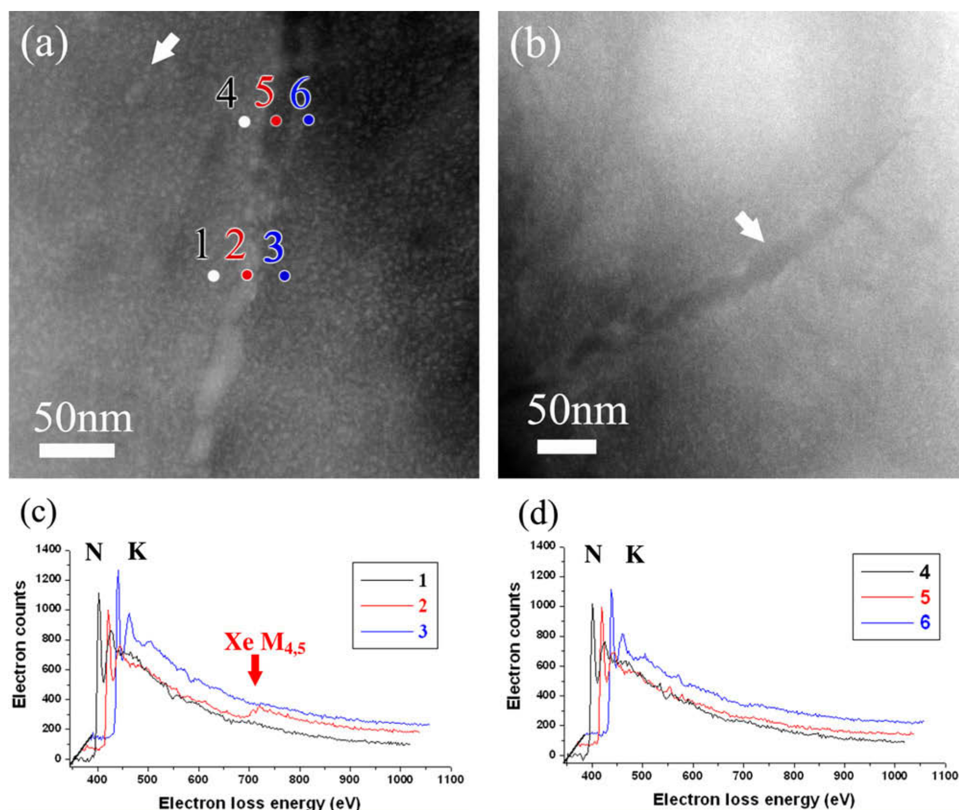

Fig. 3. (a and b) HAADF-STEM images and (c and d) EEL spectra of positions 1–6 in (a). The Z-contrast image clearly shows the Xe precipitates at the GB and the sites where they evaporate.

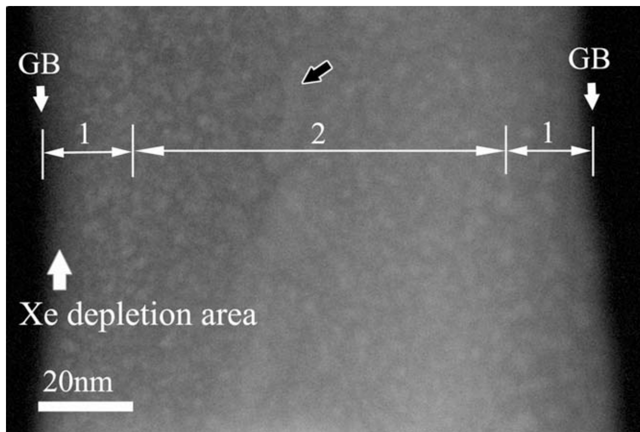

Fig. 4. HAADF-STEM image of a single grain.

precipitates at the GB in an Al matrix was reported [6]. The faceted plane corresponds to the low-surface-energy plane of Si_3N_4. Precipitates grow faster at the GB than in grains because of the diffusion of Xe from the area close to the GB. If adjacent Xe precipitates at the GB meet each other, coalescence should occur. Coalescence also occurs in grains. In our experimental results shown in Figs. 3a and 4, coarse Xe precipitates formed at the GB and near the center of the grain due to the coalescence of adjacent Xe precipitates, respectively. These results coincide well with the behavior of Xe precipitation displayed in Fig. 5.

In this model, we omitted the diffusion of Xe to the thin foil surface. However, the diffusion to the sample surface is also important in the thin foil implantation. During annealing at 800 °C, Xe which located in the close area would be diffuse out via the thin foil surface such as Figs. 2c and 3b. We estimated indirectly the moving distance (7–10 nm) of Xe, that was the Xe-depleted width from the GB in Fig. 4, in Si_3N_4 matrix. From the result of SRIM calculation (stopping ranges of implanted Xe; 26–40 nm), the implanted Xe would be mainly located in the thickness range from 26 to 40 nm. If we consider the moving distance (7 nm, the minimum Xe-depleted width) from the implanted depth during annealing at 800 °C, the Xe position in the sample can be calculated from 33 nm to 47 nm. Therefore, we can predict that the implanted Xe will be evaporated during annealing in the thin area below the thickness about 33 nm. We investigated sample thickness of the same areas with Fig. 2a and c using EEL spectra [18]. The area of Fig. 2a was revealed about 107 nm thickness. This is thick enough of Xe to remain inside of Si_3N_4 matrix. However, the vicinity of the bright area (denoted by white arrow) in Fig. 2c was measured to about 32 nm thickness. Xe will be diffuse out to the thin foil surface in this case. The thickness of the black arrow area in Fig. 2c was about 36 nm. There is the possibility of Xe to stay inside of the thin foil in this thickness. In our observation, every thin area was not detected Xe even though the particle shapes in size of about 20 nm were remained in the matrix. This clarifies the diffusion of Xe from the inside of sample to the thin foil surface in thin area.

4.2. Effect of Xe precipitation at GBs on the fracture strength

The detrimental effects of Xe precipitation at GBs on the mechanical properties were evaluated through investigating the formation and propagation of crack. In Fig. 3b, we identified the formation of a crack on the surface of Si_3N_4 upon Xe irradiation at a high temperature. The effect of crack size on the fracture strength has been extensively reported [22]; the fracture strength is inversely proportional to the square root of crack length. Therefore, it is obvious that the existence of this crack can decrease the fracture strength.

To examine the effect of Xe precipitation at GBs on crack propagation in polycrystalline Si_3N_4, we indented the TEM samples surface that had and had not undergone Xe irradiation using a manipulator attached with a diamond scriber. The force was applied to the normal direction of the thin foil surface at thick area around an edge in the TEM sample. This is similar with the conventional indentation method using a Vickers Hardness [23]. The crack was propagated across the thin center area of the sample during applying force and finally reached to the opposite edge. Crack paths on the TEM sample surfaces were observed by SEM specifically around the center areas which had a little distance from the indentation location. Fig. 6a andb shows the crack paths of the samples after heating at 800 °C for 56 min without and with Xe irradiation, respectively. To eliminate the effect of annealing on crack propagation, the unirradiated sample was also annealed at 800 °C for 56 min. In the case of no irradiation by Xe, the crack path was almost straight. In Fig. 6a, it is clear that the fracture morphol-

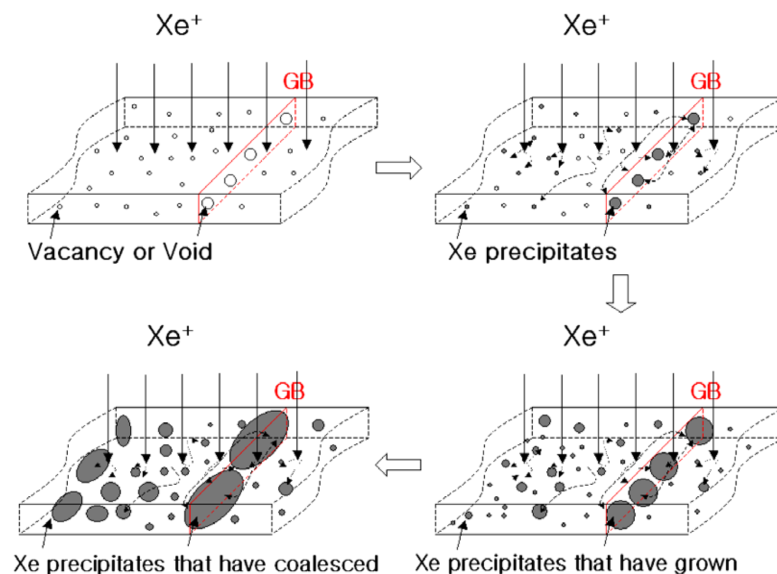

Fig. 5. Mechanism of Xe precipitation in a grain and at a GB.

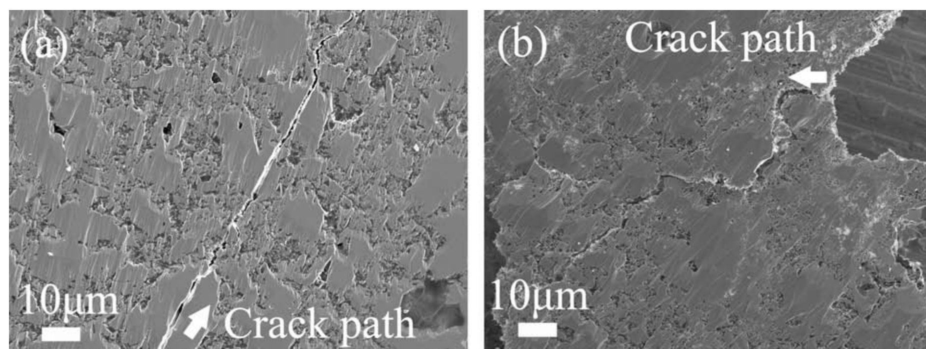

Fig. 6. Crack paths of Si_3N_4 samples after heating at 800 °C for 56 min (a) without and (b) with Xe irradiation. The crack path was almost straight in the sample without Xe irradiation. However, wavy crack propagation occurred in the Xe-irradiated sample.

ogy is both transgranular and intergranular. Large grains of about 10 μm in size exhibit transgranular fracture but small grains exhibit intergranular fracture. In contrast, wavy crack propagation is apparent in the Xe-irradiated sample as shown in Fig. 6b, in which intergranular fracture is dominant. Although there have been reports that the GBs between large grains cannot certainly be the crack path in high-temperature sintered Si_3N_4 [24,25], our results suggest that the ratio of intergranular fracture to transgranular fracture was clearly increased by the effect of Xe precipitation at the GBs.

Although the Xe precipitates are in a fluid state and accommodate the local stress at the GB, the precipitation of Xe at the GB has the role of breaking inter grain bonding in Si_3N_4 at the GB. It is known that an amorphous intergranular glassy film between Si_3N_4 grains often weakens the inter grain bonding since it generates dangling bonds at the interface [26]. When the amorphous layer is replaced with Xe precipitates, the inter grain bonding should also be weakened and Xe-precipitation-induced stress is expected to occur at the GB, resulting in the GB becoming a crack propagation path.

5. Conclusion

The precipitation of Xe at GBs was investigated in Si_3N_4 ceramic. Xe precipitates of size 5–50 nm and voids at the GB were identified by EFTEM mapping and the observation of EEL spectra. The Xe precipitates was revealed to be in the amorphous state. A model of Xe precipitation in Si_3N_4 ceramic was suggested on the basis of HAADF-STEM observations. The detrimental effect of Xe precipitation at GBs on the fracture strength was discussed from the viewpoints of crack generation and crack propagation due to the evaporation and precipitation of Xe at the GBs, respectively. The Xe precipitates at the GBs triggered intergranular fracture owing to their role in weakening the inter grain bonding at the GBs.

Acknowledgement

This study was partly financially supported by the Budget for Nuclear Research of the Ministry of Education, Culture, Sports, Science and Technology, based on screening and counseling by the Atomic Energy Commission.

References

[1] C. Templier, H. Garem, J.P. Riviere, Philos. Mag. A 53 (1986) 667–675.
[2] I. Sakamoto, N. Hayashi, B. Furubayashi, H. Tanoue, J. Nucl. Mater. 179–181 (1991) 1053–1056.
[3] O. Okada, K. Nakata, S. Kasahara, J. Nucl. Mater. 265 (1999) 232–239.
[4] C.H. Zhang, J. Jang, M.C. Kim, H.D. Cho, Y.T. Yang, Y.M. Sun, J. Nucl. Mater. 375 (2008) 185–191.
[5] R.C. Birtcher, S.E. Donnelly, C. Templier, Phys. Rev. B 50 (1994) 764–769.
[6] C.W. Allen, M. Song, K. Furuya, R.C. Birtcher, K. Mitsuishi, U. Dahmen, J. Electron Microsc. 48 (1999) 503–509.
[7] A. vom Felde, J. Fink, T.M. Heinzerling, J. Pflüger, B. Scheerer, G. Linker, D. Kaletta, Phys. Rev. Lett. 53 (1984) 922–925.
[8] J.H. Evans, D.J. Mazey, Scripta Metall. 19 (1985) 621–623.
[9] M.G. Norton, E.L. Fleischer, W. Hertl, C.B. Carter, J.W. Mayer, E. Johnson, Phys. Rev. B 43 (1991) 9291–9294.
[10] M. Song, X. Guo, N. Ishikawa, M. Takeguchi, K. Mitsuishi, K. Furuya, Mater. Sci. Forum 561–565 (2007) 1757–1760.
[11] F. Li, P. Lu, K.E. Sickafus, J. Nucl. Mater. 306 (2002) 121–125.
[12] C.H. Zhang, Y.M. Sun, Y. Song, T. Shibayama, Y.F. Jin, L.H. Zhou, Nucl. Instrum. Methods Phys. Res. B 256 (2007) 243–247.
[13] M.G. Norton, C.B. Carter, E.L. Fleischer, J.W. Mayer, J. Mater. Res. 7 (1992) 3171–3174.
[14] C.W. White, C.J. McHargue, P.S. Sklad, L.A. Boatner, G.C. Farlow, Mater. Sci. Rep. 4 (1989) 41–146.
[15] K. Iakoubowskii, K. Mitsuishi, K. Furuya, Phys. Rev. B 78 (2008) 064105-1–064105-6.
[16] N. Ishikawa, K. Furuya, Ultramicroscopy 56 (1994) 211–215.
[17] J.F. Ziegler, J.P. Biersack, U. Littmark, The Stopping Range of Ions in Solids, Pergamon, New York, 1985.
[18] R.F. Egerton, S.C. Cheng, Ultramicroscopy 21 (1987) 231–244.
[19] C.M. Wang, J. Am. Ceram. Soc. 78 (1995) 3393–3396.
[20] T. Hehenkamp, W. Berger, J.E. Kluin, C. Lüdecke, J. Wolff, Phys. Rev. B 45 (1992) 1998–2003.
[21] T. Yano, M. Akiyoshi, K. Ichikawa, Y. Tachi, T. Iseki, J. Nucl. Mater. 289 (2001) 102–109.
[22] G.E. Dieter, Mechanical Metallurgy, third ed., McGraw-Hill, London, 1988.
[23] R.F. Cook, G.M. Pharr, J. Am. Ceram. Soc. 73 (1990) 787–817.
[24] H.-J. Kleebe, G. Pezzotti, G. Ziegler, J. Am. Ceram. Soc. 82 (1999) 1857–1867.
[25] P.F. Becher, J. Am. Ceram. Soc. 74 (1991) 255–269.
[26] S. Ii, C. Iwamoto, K. Matsunaga, T. Yamamoto, Y. Ikuhara, J. Electron Microsc. 53 (2004) 121–127.